Intermetallics 139 (2021) 107367

Contents lists available at ScienceDirect

Intermetallics

journal homepage: www.elsevier.com/locate/intermet

Correlation of microstructure and mechanical properties of Ti_2AlNb manufactured by SLM and heat treatment

Xiuxuan Yang [a], Bi Zhang [b], Qian Bai [a,*], Guoyin Xie [c]

[a] Key Laboratory for Precision and Non-traditional Machining Technology of Ministry of Education, Dalian University of Technology, Dalian 116024, China
[b] Department of Mechanical and Energy Engineering, Southern University of Science and Technology, Shenzhen 518055, China
[c] AECC Xi'an Aero-Engine Ltd., Xi'an 710021, China

ARTICLE INFO

Keywords:
Selective laser melting
Ti_2AlNb intermetallic
Heat treatment
Microstructural characteristic
High-temperature tensile properties

ABSTRACT

Ti_2AlNb intermetallic has a promising application in aeronautics and aerospace industries due to its high strength-to-weight ratio and high creep resistance at an elevated temperature. Selective laser melting (SLM) of this material has been emerging recently. The correlation of its microstructure and mechanical properties after the SLM and heat treatment determines the application of this material. In this paper, the process window of SLM for Ti_2AlNb was determined. Characteristics of lath, acicular and grain boundary (GB) precipitates were studied after different heat treatments. The relation of solution heat treatment (SHT) temperature on the size and volume fraction of precipitates before and after aging treatment (AT) were established. High-temperature tensile test of the SLMed and heat-treated intermetallic were conducted. A relation between microstructure and mechanical properties was proposed. The change of the tensile strength and elongation at elevated temperature were rationalized. The results show that for the SLMed sample the dominating B2 phase led to a good room temperature ductility, but at 650 °C the continuous precipitation along the GB deteriorated the tensile strength and ductility. After SHT (920 °C) + AT, the maximum elongation (El) at 650 °C was significantly increased due to the precipitation of large-sized lath O+α_2 phase. After SHT (1000 °C) + AT, the maximum ultimate tensile strength (UTS) of the tensile test at 650 °C increased to 820 MPa due to the precipitated acicular O phase.

1. Introduction

Ti_2AlNb intermetallic presents superior properties such as high strength-to-weight ratio and high creep resistance at elevated temperature. Hence, the Ti_2AlNb intermetallic have received considerable attention as potential advanced materials in aeronautics and aerospace industries. In the past few years, forging [1], hot isostatic pressing [2], and powder metallurgy [3], etc. have been investigated to prepare Ti_2AlNb intermetallic. It had been suggested that there were B2 matrix, O phase and α_2 phase in the prepared Ti_2AlNb [4]. Among them, the presence of B2 matrix phase (ordered structure) is essential in imparting ductility and toughness of Ti_2AlNb [5]. The O phase (orthorhombic structure) is known to increase creep resistance and strength for Ti_2AlNb [6]. The existence of α_2 phase (hexagonal close-packed structure) is beneficial to hindering the B2 grain growth [7]. The volume fraction and morphology of those phases were usually controlled by heat treatment process, which could enhance the high temperature strength and creep resistance of Ti_2AlNb. However, due to its poor ductility at room temperature and the weak formability at elevated temperature, it is difficult to fabricate complex shaped Ti_2AlNb parts, which limited its industrial applications.

Selective laser melting (SLM) is capable of fabricating parts with complex geometry, achieving near net-shaping and customization without the need for expensive tooling or molds [8–10]. In recent years, some researchers studied SLM process of Ti_2AlNb-based intermetallic. Grigoriev et al. [11] used elemental powder mixtures of Ti–22Al–25Nb and obtained the SLMed samples with the highest relative density of 99.5%. Zhou et al. [12] used pre-alloyed powders of Ti–22Al–25Nb in SLM, and found that the high strength and large ductility of the SLMed samples at room temperature were attributed to the disordered β phase and a very small amount of nano-scale O phase. For Ti_2AlNb intermetallic, a material utilized at elevated temperature, its high temperature mechanical properties are important to the applications. Generally, O phase in Ti_2AlNb plays a dominating role to improve the creep resistance and strength, but in the SLMed Ti_2AlNb, there was mainly B2 matrix phase due to the ultra-rapid heating and cooling [12]. Therefore, heat

* Corresponding author.
E-mail address: baiqian@dlut.edu.cn (Q. Bai).

https://doi.org/10.1016/j.intermet.2021.107367
Received 30 May 2021; Received in revised form 6 September 2021; Accepted 12 September 2021
Available online 17 September 2021

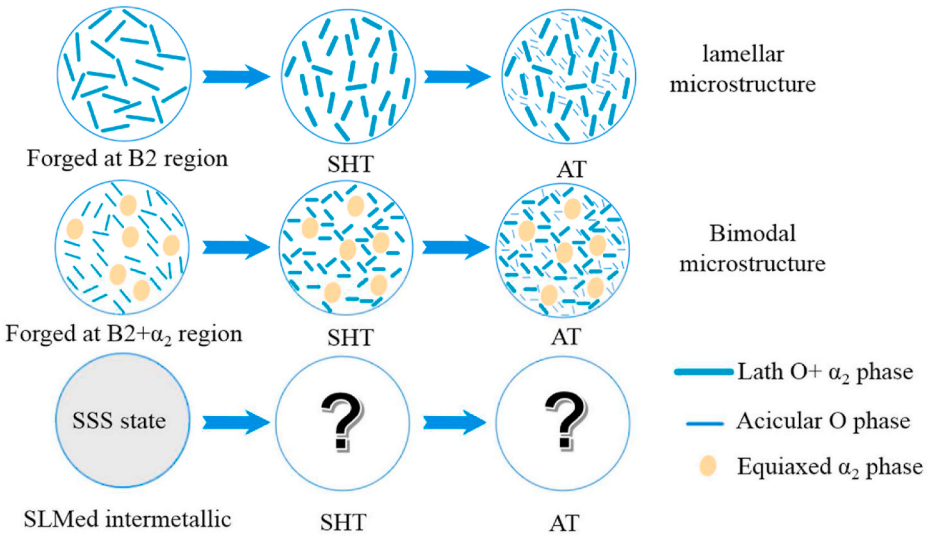

Fig. 1. Schematic of microstructure evolution in heat treatment of Ti_2AlNb.

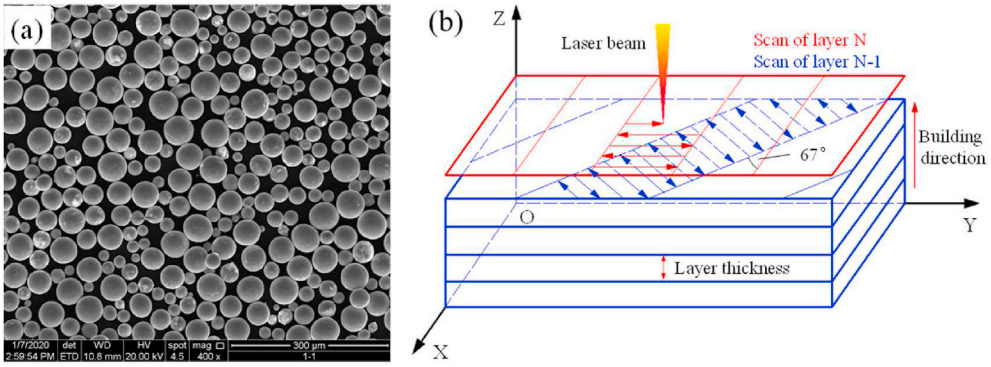

Fig. 2. (a) Spherical morphology of the pre-alloyed Ti–22Al–24Nb-0.5Mo powder; (b) the schematic of the strip scanning strategy used to fabricate Ti_2AlNb specimens by SLM.

Table 1
SLM processing parameters used in this study.

Laser power (W)	Scanning speed (mm/s)	Layer thickness (μm)	Hatch distance (μm)
80–280	200-1000	30	100

Table 2
SHT temperature of the SLMed intermetallic.

	T_{S1}	T_{S2}	T_{S3}	T_{S4}	T_{S5}	T_{S6}	T_{S7}	T_{S8}
T (°C)	1090	1020	1000	980	960	940	920	880

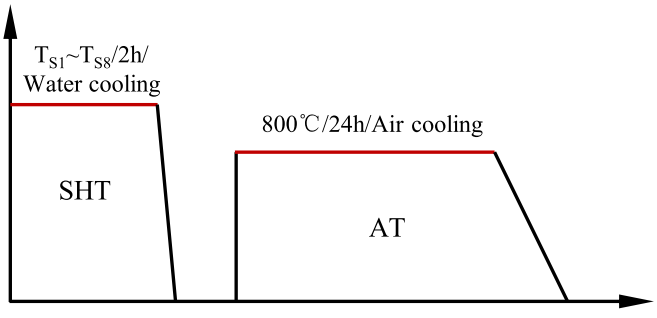

Fig. 3. Heat treatment of the SLMed intermetallic.

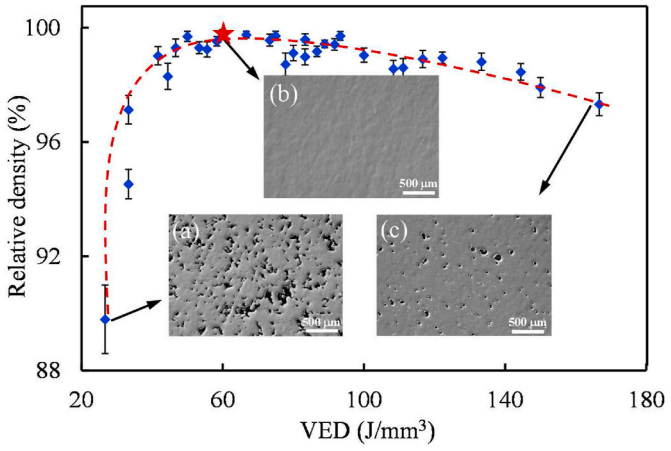

Fig. 4. Relationship between relative density and VED, (a) P = 180 W, v = 1000 mm/s, (b) P = 80 W, v = 1000 mm/s, (c) P = 200 W, v = 400 mm/s.

treatment after SLM is essential to improve the mechanical properties.

To date, several studies on heat treatment of Ti_2AlNb had been conducted in various processes, such as forging [13,14], hot isostatic

Table 3
Chemical compositions of Ti–22Al–24Nb-0.5Mo (at. %) of SLMed samples.

	Al	Nb	Mo	Ti
Nominal	22	24	0.5	Bal.
Powder	21.68	25.02	0.59	Bal.
Sample (a)	21.24	24.78	0.57	Bal.
Sample (b)	20.63	25.04	0.57	Bal.
Sample (c)	20.09	25.87	0.61	Bal.

pressing [15], and laser-welding [16]. Ti_2AlNb, as a multiphase intermetallic, contains B2 matrix phase, α_2 phase and O phase. The volume fraction and morphology of these constituent phases are sensitive to the forming process and heat treatment process. Therefore, the microstructure of Ti_2AlNb is complex and difficult to control [17]. As shown in Fig. 1, when the material was isothermally forged in B2 phase region, lath O+α_2 was generated, while forged in B2+α_2 phase region, equiaxed α_2 and small-sized lath O+α_2 were obtained [18]. In SHT, lath O+α_2 was coarsened at high temperature. After AT, acicular O phase was precipitated. Therefore, the different initial microstructures of a forged material led to lamellar and bimodal microstructure respectively after heat treatment. The SLMed materials were in supersaturated solid solution (SSS) state due to the rapid cooling rate [19], which was different from the forged microstructure. Therefore, the heat treatment procedure of the forged parts is not applicable to the SLMed ones. Zhou [20] et al. studied the effects of SHT temperature (950 °C, 1050 °C and 1100 °C) and aging temperature (700 °C and 830 °C) on the microstructure and mechanical properties of the SLMed Ti–22Al–25Nb. For high-temperature tensile properties, the maximum elongation (El) was 10% after SHT950 °C + AT830 °C with UTS of 611 MPa, and the maximum UTS was 749 MPa after SHT950 °C + AT700 °C with El of 1.6%. However, a quantitative analysis on the effects of heat treatment on the volume fraction and size of the precipitated phases of the SLMed Ti_2AlNb is still lack of study.

In this study, the Ti–22Al–24Nb-0.5Mo (at. %) intermetallic samples were fabricated using SLM. The process window of SLM was obtained in terms of the relative density. The influences of heat treatment on the volume fraction and size of the precipitated phases were analyzed quantitatively. Correlation between the microstructure and high-temperature tensile properties was also studied for SLMed intermetallic.

2. Experiments

2.1. SLM process of Ti_2AlNb intermetallic

In this study, the SLMed Ti–22Al–24Nb-0.5Mo (at. %) specimens were fabricated from the pre-alloyed Ti–22Al–24Nb-0.5Mo (at. %) powder. The SEM micrograph of the powder as shown in Fig. 2 (a). The diameter of the powder was between 15 μm and 53 μm. High-purity argon gas was used during the SLM process to prevent oxidation [21, 22]. Phase compositions of the SLMed intermetallic were characterized using X-ray diffraction (XRD, Empyrean, Netherlands) with a Cu Kα radiation and a step size of 0.01°. The chemical composition of the powder and SLMed samples were measured by inductive coupled plasma

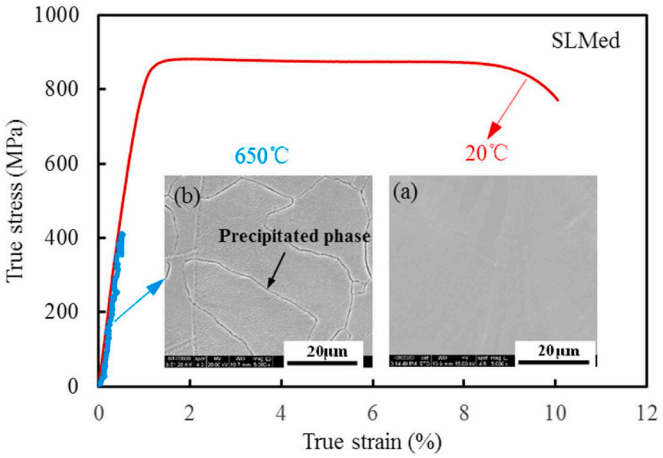

Fig. 6. Representative tensile true stress-strain curves of the SLMed Ti_2AlNb samples at room temperature and elevated temperature (650 °C).

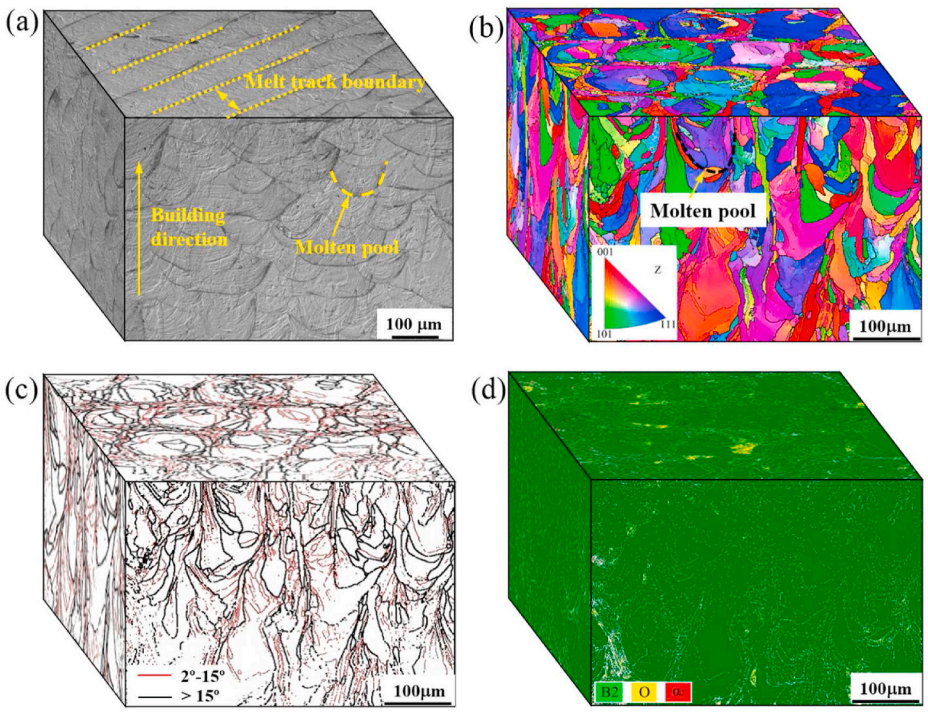

Fig. 5. Microstructure and phase composition of the SLMed Ti–22Al–24Nb-0.5Mo intermetallic, (a) OM picture, (b) IPF map, (c) GB map, (d) phase map.

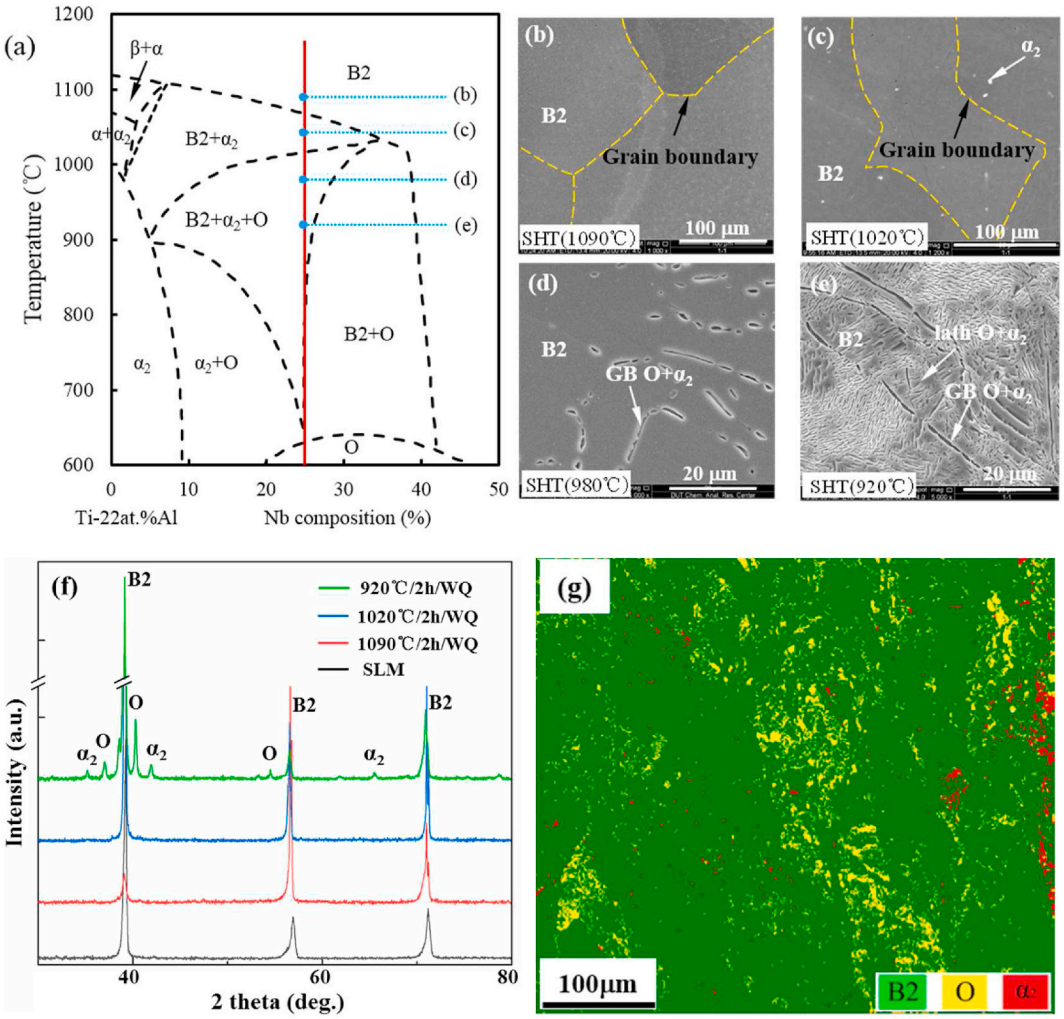

Fig. 7. (a) The pseudo-binary phase diagram for Ti–22Al-xNb (at. %), (b–e) the microstructure and (f) XRD results of the SLMed Ti_2AlNb samples at different SHT temperatures, (g) the phase map of EBSD for SHTed sample at 980 °C.

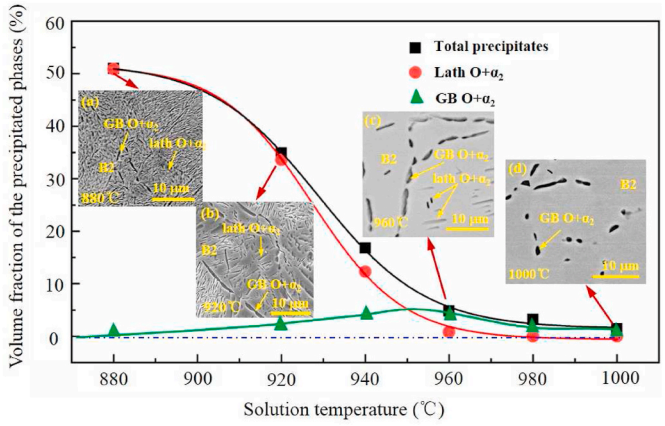

Fig. 8. Effects of SHT temperature on the volume fraction of precipitated phases.

optical emission spectrometer (ICP-OES, Aglient 5110, America). The schematic diagram of the scanning strategy is presented in Fig. 2b. Strip scanning strategy was adopted in this paper to reduce the residual stress in the SLM samples [23,24]. The stripe angle between the adjacent layers (N and N-1) was 67°. The laser spot size was about 80 μm. The SLM process parameters used is shown in Table 1. The fixed interval of laser power in Table 1 was 20 W, and the fixed interval of scanning speed was 200 mm/s. The layer thickness and hatch distance were kept constant as shown in Table 1.

The SLMed samples were polished and their relative density were measured by the Archimedes method. Seven times were measured to obtain the average relative density in this paper. As shown in Eq. (1), volume energy density (VED) was defined to evaluate the manufacturing quality in terms of relative density [25],

$$VED = \frac{P}{v^* d^* h} \tag{1}$$

where P is laser power; v is scanning speed; d is hatch distance; and h is layer thickness.

2.2. Heat treatment of the SLMed samples

According to the previous studies of other researchers, the SHT process mainly influenced the volume fraction of precipitated phases, and the size of the initial lath O+α_2 phase [26]. Therefore, this paper focused on the effect of SHT on microstructure. As shown in Fig. 3, the SLMed samples were SHTed at different phase regions for 2 h first, water cooled, and then aged at 800 °C for 24 h followed by air cooling. SHT temperatures were selected as shown in Table 2. The heat treatment process was carried out in a vacuum heat treatment furnace with a

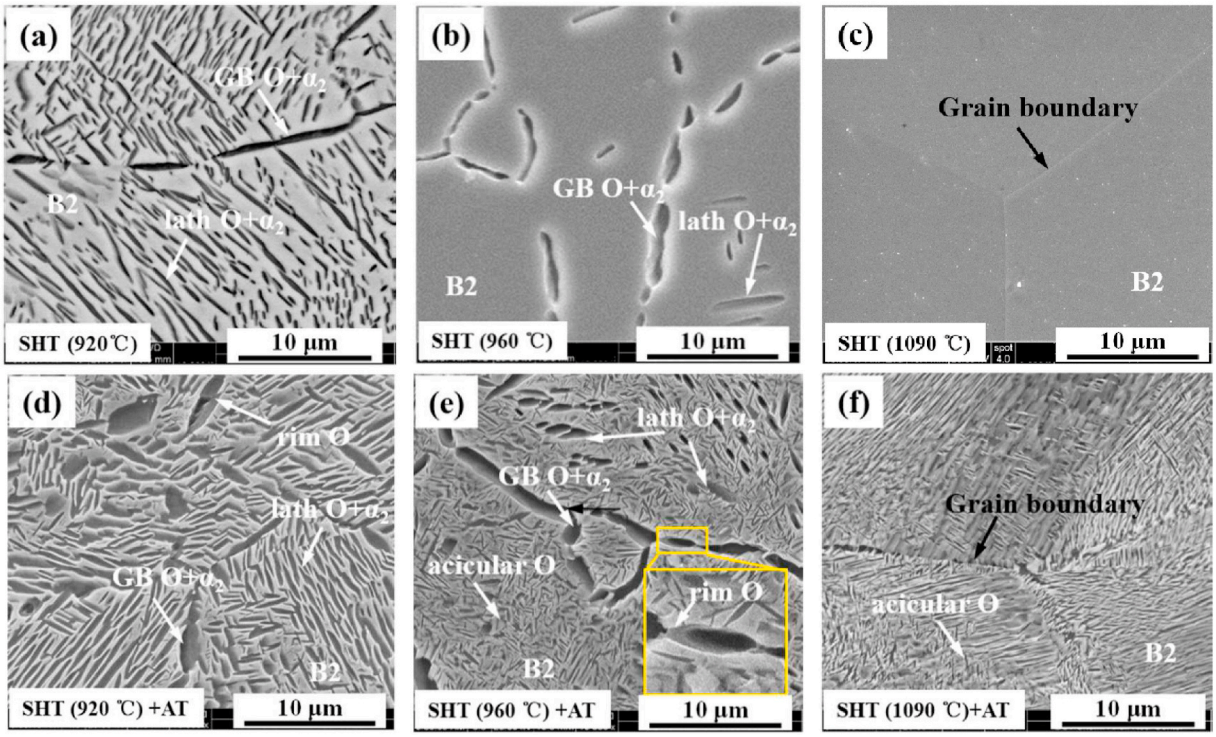

Fig. 9. Microstructure of the SLMed samples with different SHT temperatures (a) 920 °C after SHT, (b) 960 °C after SHT, (c) 1090 °C after SHT, (d) 920 °C after SHT + AT, (e) 960 °C after SHT + AT, (f) 1090 °C after SHT + AT.

vacuum degree of 5×10^{-3} Pa. The SLMed and heat-treated samples were ground with abrasive paper to remove the oxide layer on the surface, polished with silica sol, and then etched with Keller's reagent for 40s (5%HF+10%HNO_3+H_2O). We observed the microstructure of the SLMed and heat-treated samples using scanning electron microscopy (SEM, ZEISS, Germany), backscattered electron (BSE), and Electron Backscattered Diffraction (EBSD), respectively.

Three SEM images were selected for each test condition. The volume fraction of the precipitated phases was calculated using MATLAB. The average lath length and width were measured by Image-Pro Plus software. Room-temperature (20 °C) and high-temperature tensile (650 °C) experiments were conducted at a constant strain rate of $0.001s^{-1}$. The tensile samples were deformed in the direction perpendicular to the building direction, and were tested three times to obtain the average results. The effects of heat treatment on the ultimate tensile strength (UTS) and elongation (El) of the materials were studied.

3. Results and discussion

3.1. SLM results of the Ti–22Al–24Nb-0.5Mo intermetallic

Fig. 4 shows the relation of VED and the relative densities of the SLMed samples. The chemical composition of the powder and SLMed samples at different VED was measured by ICP-OES, and the results are shown in Table 3. The chemical compositions of the powder were basically consistent with the nominal values. At a lower VED of 26.67 J/mm^3, due to the insufficient melting of the powder, there were a large number of lack of fusion defects in the SLMed sample (a), resulting in a low relative density, which was also reported in Ref. [27]. The content of Al element in sample (a) was 21.24 at.% and was less than that in the powder (21.68 at.%), indicating that the loss of low melting temperature element was inevitable. As the VED increased, the powder melted sufficiently and the relative density was increased, and then reached the largest value at about VED = 60J/mm^3 for sample (b). There were no obvious defects in the sample (b). The content of Al element in sample (b) decreased to 20.63 at.% due to the increase of VED. After that, the relative density decreased with the VED, which was attributed to the fact that the excessive energy density vaporized the material and thus caused keyhole defects [28,29]. As shown in Table 3, due to the excessive energy density vaporized the Al element, its content in sample (c) was decreased to 20.09 at.%. Considering the quality of the SLMed samples and the processing efficiency, the optimized scanning speed was 1000 mm/s, and power was 180 W. The relative density reached 99.8% of the theoretical density.

The microstructure of the SLMed samples is shown in Fig. 5. The molten pool morphology (Fig. 5a) corresponded to the microstructure characteristic of the SLMed samples (Fig. 5 b and c), indicating no obvious epitaxial grain growth during the SLM process. This is due to the fact that the high content of solute elements in Ti_2AlNb retarded the grain growth during the solidification of SLM. Therefore, the SLMed samples could be considered as isotropic. The GB results in Fig. 5c show that grains of the SLMed samples were irregular, and the grain size in the central area of the melt tracks was about 100 μm, which was much larger than that in the melt track boundary. It is attributed to the fact that low temperature gradient and solidification rate resulted in a larger grain growth rate in the central area than that at the boundary of the melt track [30]. Due to the rapid cooling rate of the SLM, a large number of low-angle grain boundaries (LAGBs, 2°–15°) existed along the melt track boundary. An EBSD phase map of the SLMed samples in Fig. 5d shows that the SLMed samples mainly consisted of the B2 matrix, in addition to a small amount of O phase. This O phase was considered to be in a nano state, according to Zhou's study [12]. No α_2 phase was found in the SLMed samples.

Fig. 6 shows the tensile properties of the SLMed samples at room temperature and elevated temperature (650 °C). In the room temperature tensile test, the SLMed samples were in the SSS state (Fig. 6a), and thus the material possessed a UTS of 900 MPa and an El of 9%. However, in the elevated temperature tensile test, precipitated phases were distributed continuously along the grain boundaries as shown in Fig. 6b, resulting in a poor ductility. Therefore, the SLMed Ti_2AlNb sample parts

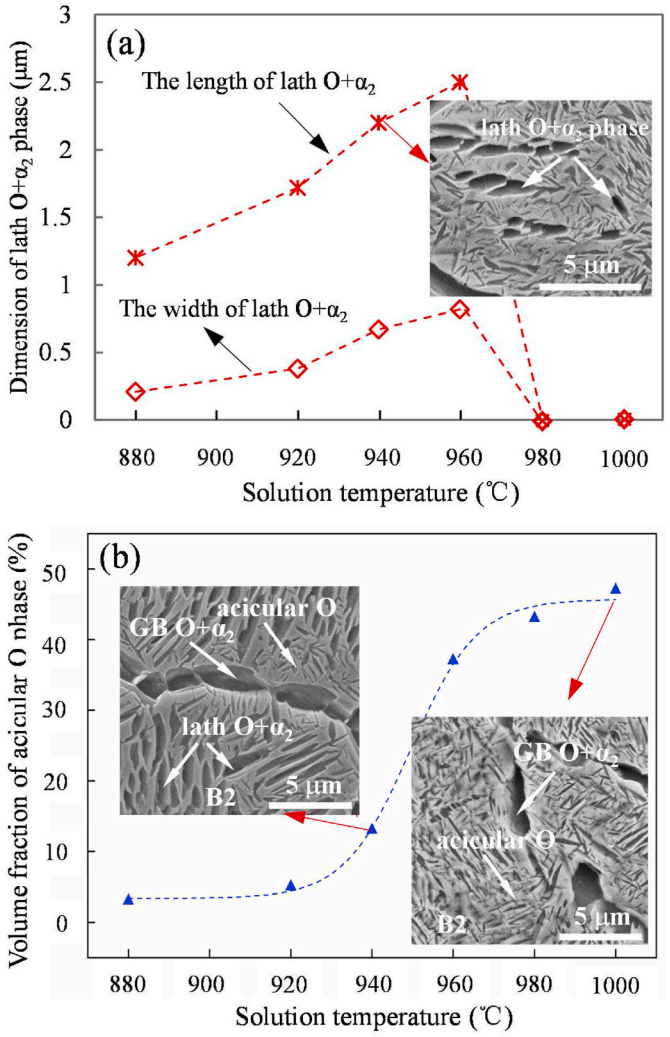

Fig. 10. Effects of SHT temperature on (a) the dimension of lath O+α_2, (b) the volume fraction of acicular O phase.

cannot be used directly, and heat treatment is necessary before service at elevated temperatures.

3.2. SHT temperature effects on the microstructure

According to the pseudo-binary phase diagram for Ti–22Al-xNb (at. %) in Fig. 7a [31], the SLMed samples were solution heat treated at different temperatures in terms of phase regions. When SHT temperature was at the single-phase region (1090 °C), B2 matrix existed dominatingly, and the grain size of B2 was larger than 200 μm due to the lack of pinning effect by the precipitates (Fig. 7b and f). When SHT temperature was at B2+α_2 phase region (1020 °C), the equiaxed grains of B2 mainly existed with a small amount of α_2 phase (Fig. 7c). The grain size was also larger than 200 μm, since the volume fraction of α_2 phase was too small to hinder the grain growth, which was consistent with the XRD results in Fig. 7f. When SHT temperature was at B2+O+α_2 phase region (980 °C), the grain boundary can provide energy for the precipitates, as a result, the α_2 phase and O phase were precipitated along the grain boundaries, named as GB O+α_2 (Fig. 7d). Apart from GB O+α_2, small size of O+α_2 was also distributed dispersedly within the material (Fig. 7g). When SHT temperature was 920 °C, B2, GB O+α_2 and lath O+α_2 were found in the SHTed sample (Fig. 7e and f).

The effects of SHT temperature on the volume fraction of the precipitated phases, i.e., lath O+α_2 and GB O+α_2 were illustrated in Fig. 8. As the solubility of the solutes increased with the SHT

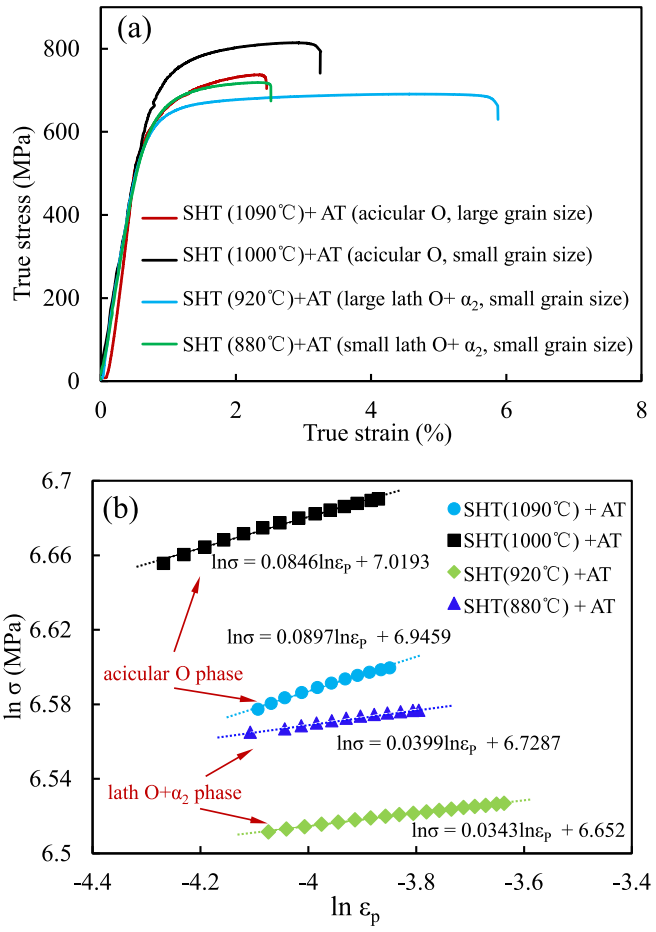

Fig. 11. (a) High temperature (650 °C) strain-stress curves after SHT + AT, (b) log-log plot of true strain-stress curves.

temperature [32], the volume fraction of the lath O+α_2 and the total precipitated phase decreased with the SHT temperature. When the SHT temperature was ranged from 880 °C to 920 °C, lath O+α_2 was precipitated with a volume fraction from 50% to 35% (Fig. 8a and b). Since the SHT temperature was close to the B2+O phase region, less amount of the α_2 phase was precipitated at the grain boundaries, and thus discontinuous GB O+α_2 generated along the grain boundary. When the SHT temperature was ranged from 920 °C to 960 °C, the volume fraction of GB O+α_2 increased slightly, and the discontinuous GB O+α_2 was changed to continuous one with the increase of the SHT temperature (Fig. 8c). At SHT 1000 °C, no lath O+α_2 was precipitated (Fig. 8d). The continuous GB O+α_2 changed to discontinuous one since the volume fraction of GB O+α_2 was decreased at high temperatures. Based on Fig. 8, the relation between the volume fraction of lath O+α_2 V_L and the SHT temperature T_S is expressed as

$$\lg\left(\frac{V_{L0}}{V_L} - 1\right) = A^* T_S - B \tag{2}$$

where V_{L0} is the volume fraction of the lath O+α_2 at SHT 880 °C (*i.e.* 52 %), A was 0.04, and B was 37.

3.3. Microstructures and mechanical properties after SHT + AT

The microstructure of the SHTed samples before and after AT was shown in Fig. 9. When SHT temperature was 920 °C, there were GB O+α_2 and a large amount of lath O+α_2 precipitated (Fig. 9a), little acicular O phase was observed after AT (Fig. 9d). When SHT temperature was 960 °C, the volume fraction of lath O+α_2 decreased

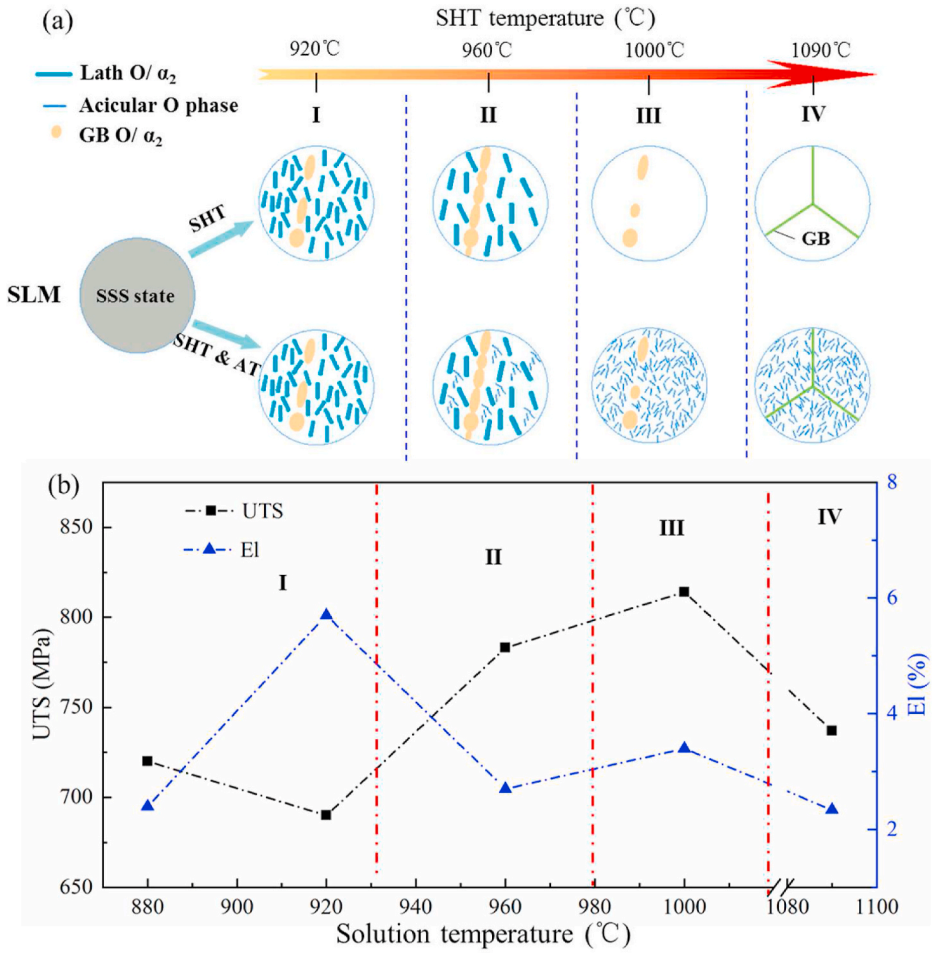

Fig. 12. (a) The schematic diagram of microstructure changes at different SHT temperatures after SHT and SHT + AT; (b) effects of SHT temperature on the high-temperature tensile properties of the SLMed Ti_2AlNb after SHT + AT.

significantly, but its size increased compared with the SHT temperature of 920 °C (Fig. 9b). After AT, a large amount of acicular O phase was transformed from B2 matrix (Fig. 9e), and its acicular shape may be caused by the low-energy configuration for specific sets of planes in the O and B2 phases [33].When SHT temperature was1,090 °C, only B2 matrix was generated in the sample (Fig. 9c). After the AT a large amount of acicular O phase was precipitated in Fig. 9f. It is also noted that in Fig. 9d and e, after AT, rim-O phase was formed around α_2 phase at grain boundaries via B2 + $\alpha_2 \rightarrow$O reaction [34], and some α_2 phases were transformed into O phase completely [35].

After AT, the effects of SHT temperature on the precipitated phases (*i.e.* lath O+α_2, acicular O phase and GB O+α_2) were shown in Fig. 10. Because the higher temperature provided more active energy to the diffusion process to help the lath O+α_2 growth [36], the width and length of the lath O+α_2 phase increased with the SHT temperature in the range of 880 °C–960 °C (Fig. 10a). When SHT temperature was higher than 960 °C, little lath O+α_2 existed in the material. The volume fraction of the lath O+α_2 had no obvious changes before and after AT, as shown in Fig. 9. Therefore, it was indicated that the volume fraction and size of the lath O+α_2 were mainly controlled by the SHT process.

For the acicular O phase, after AT the volume fraction increased with the SHT temperature (Fig. 10 b), which is contrary to the changes of the lath O+α_2 (Fig. 8). This is because when a large amount of lath O+α_2 was precipitated after SHT (*e.g.* SHTed at 920 °C), many solute atoms were consumed, hindering the acicular O phase during AT. In contrast, when little lath O+α_2 was precipitated after SHT (*e.g.* SHTed at 960 °C), a large number of solute atoms were still solidly dissolved in the material, and acicular O phase precipitated after AT. Therefore, the acicular O phase was generally precipitated after AT, but its volume fraction was controlled by the volume fraction of lath O+α2 and the SHT temperature. The relation between the volume fraction of the acicular O phase V_A and the SHT temperature T_S can be expressed as

$$\lg\left(\frac{V_{A0}}{V_A} - 1\right) = -A^*T_S + B \tag{3}$$

where V_{A0} is the volume fraction of the acicular O phase at SHT1000 °C + AT (*i.e.* 47 %), A was 0.05, and B was 47.5.

For GB O+α_2, its continuous or discontinuous distribution along the grain boundaries was the main feature of interest compared to its volume fraction and size variation. GB O+α_2 is necessary to hinder the B2 grain growth, but the continuous GB O+α_2 may deteriorate the ductility of the material. The distribution of GB O+α_2 has no obvious changes before and after AT. When the SHT temperature was ranged from 940 °C to 980 °C, there was continuous GB O+α_2 at the grain boundary. When the SHT temperature were ranged from 880 °C to 920 °C and 960 °C to 1000 °C, there was discontinuous GB O+α_2 at the grain boundary.

The high-temperature tensile test results of the HTed samples as shown in Fig. 11a. Significant difference existed in the strain hardening exponent for the samples with mainly the acicular O phase (SHT (1090 °C) +AT, SHT (1000 °C) +AT) and the samples with mainly the lath O+α_2 (SHT (920 °C) +AT, SHT (880 °C) +AT) phase. The strain hardening exponent n of the strain-stress curves in Fig. 11a were calculated based on the power-law model as shown in Eq. (4) [37],

$$\sigma = K\varepsilon_p^n \tag{4}$$

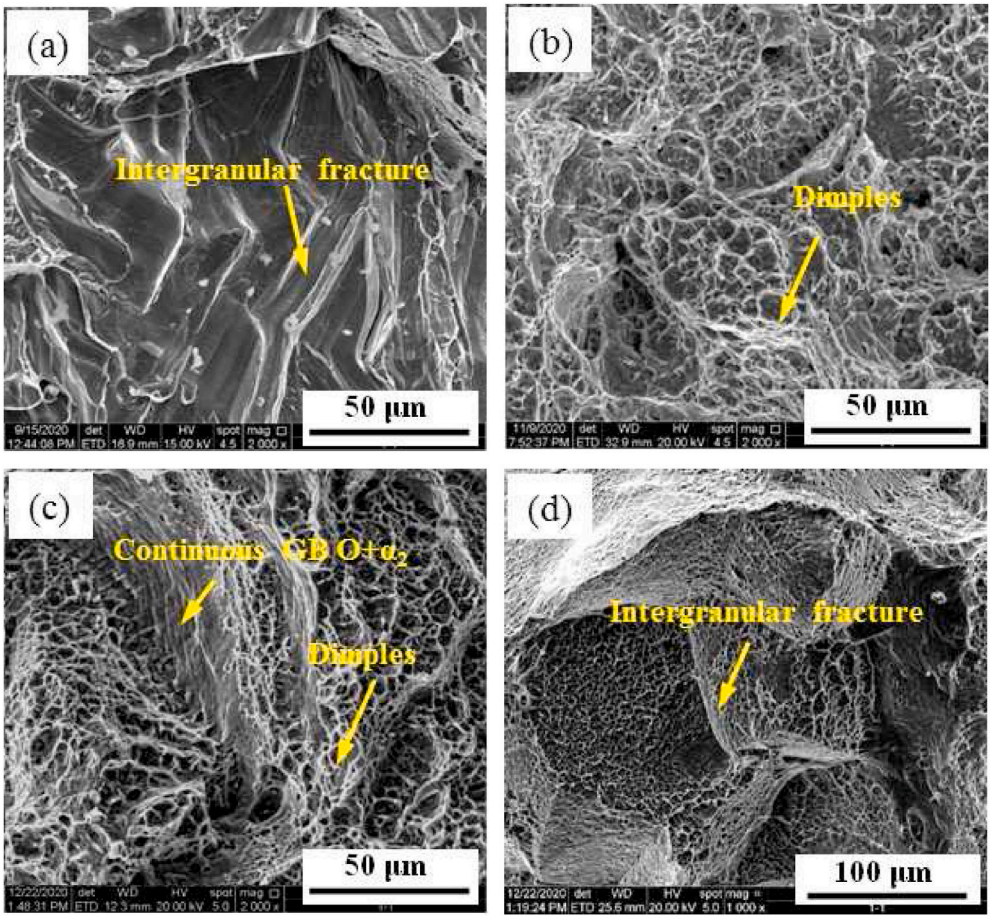

Fig. 13. Fracture surfaces of (a) tensile tested samples at 650 °C for SLMed intermetallic; and (b) heat-treated samples after SHT (920 °C) +AT; (c) SHT (960 °C) +AT; and (d) SHT (1090 °C) +AT.

Where σ and ε_p are the true stress and true plastic strain of the material at the operating temperature (650 °C), respectively. K is the strength coefficient. The true strain-stress curves on a log-log scale are shown in Fig. 11b in which n is the slope of the curves. It can be seen that the strain hardening exponent n of the material with acicular O after SHT (1090 °C)+AT and SHT(1000 °C)+AT are 0.0897 and 0.0846, respectively. The material with lath O+α_2 after SHT(920 °C)+AT and SHT (880 °C)+AT are about 0.0343 and 0.0399, respectively. The calculated strain hardening exponent n indicates that the strain hardening effect of the acicular O phase is stronger than that of lath O+α_2.

The schematic diagram of the material microstructures after different heat treatments, and the high-temperature tensile properties of the material after SHT + AT are shown in Fig. 12a and b. Based on the characteristic of the precipitates, the heat-treatment temperatures can be divided into four ranges.

In area I, there are mainly lath O+α_2 and a small amount of discontinuous GB O+α_2 before and after AT. The size of lath O+α_2 increases with the temperature (Fig. 10a); therefore, the material ductility increases but the material strength decreases according to the Hall-Petch effect [38].

In area II, there is lath O+α_2 and continuous GB O+α_2 in the samples after SHT. The acicular O phase precipitates from the matrix after AT. The precipitated acicular O phase, acting as obstacles to dislocation motions, enhances the high-temperature tensile strength of the material. However, stress concentration is likely to develop at the acicular O tips and leads to crack initiation and nucleation, which deteriorated the ductility of the material [39]. In addition, the continuous GB O+α_2 also decreased the ductility.

In area III, a small amount of discontinuous GB O+α_2 and little lath O+α_2 are generated after SHT. A large amount acicular O phase is precipitated after AT. The tensile strength of the material is larger than that in area II due to the main acicular O phase. In addition, as the distribution of GB O+α_2 changes from continuous to discontinuous, the ductility of the material is better than that in area II.

In area IV, there are large equiaxed grains with no precipitated phases in the samples after SHT. After AT, only the acicular O phase is observed. In area I, II and III, the SHT temperature is below 1000 °C, the change of grain size is small due to the precipitates of α_2 phase along the grain boundary, and thus the change in phase composition dominatingly affects the mechanical properties. When the SHT temperature is higher than 1000 °C (area IV), such as 1090 °C, the grain growth occurred due to lack of precipitation of α_2 phase along the grain boundary, reducing the strength and ductility of the material. Similar results for SHT temperatures ranging from 950 °C to 1050 °C were also observed by Zhou et al. [20].

In summary, the increased volume fraction and size of lath O+α_2 improved the ductility but deteriorated the strength of the material, while the increased volume fraction of acicular O improved the strength but deteriorated the ductility of the material. To hindering the B2 grain growth and thus improve the tensile strength, GB O+α_2 is necessary. However, the continuous GB O+α_2 should be avoided which is detrimental to ductility. As a result, to obtain a high ductility, SHT (920 °C) +AT with main lath O+α_2 and discontinuous GB O+α_2 leads to an EI of 6%. To obtain a high strength, SHT (1000 °C) +AT with main acicular O and discontinuous GB O+α_2 leads to a UTS of 800 MPa at 650 °C.

The fractography of tensile samples after SHT + AT are shown in Fig. 13. It can be seen that, as the continuous precipitated phases were along the grain boundaries, there were obvious cleavage fractures along

the grain boundary for the SLMed samples during the high-temperature tensile tests (Fig. 13a). For samples heat-treated at different temperatures, as shown in Fig. 13b and c, numerous ductile dimples were observed, indicating that the fracture mode of the heat-treated samples was predominantly ductile. The continuous precipitated GB O+α_2 phases at the grain boundary after SHT (960 °C) +AT lead to the poor ductility of the material. Fig. 13d shows the fracture surface of the material after SHT (1090 °C) +AT. Due to the large equiaxed grain size (Fig. 9f), the material possesses poor ductility and lower strength (Fig. 12b, area IV), showing a typical intergranular fracture.

4. Conclusions

In this paper, the Ti–22Al–24Nb-0.5Mo intermetallic was prepared by the SLM technique. The SLMed intermetallic was heat-treated at different SHT temperatures and a constant AT temperature (800 °C). The effects of SHT temperature on the microstructure of the SLMed samples before and after AT were studied quantitatively. Correlation of the microstructure and mechanical properties of the SLMed intermetallic after SHT + AT was investigated. Main results were obtained as follows.

1. The optimized scanning speed of the SLM process was 1000 mm/s and the power was 180 W. Due to the rapid cooling rate of the SLM process, the microstructure of the SLMed Ti_2AlNb was mainly B2 phase, in addition to a small amount of O phase.
2. The effects of SHT temperature on the precipitates (*i.e.* lath O+α_2, acicular O and GB O+α_2) were studied. With the SHT temperature increased, the volume fraction of lath O+α_2 decreased whereas the volume fraction of acicular O increased. A quantitative relationship between the volume fraction of lath O+α_2, acicular O, and the SHT temperature was established.
3. The main lath O+α_2 and discontinuous GB O+α_2 in the sample after SHT (920 °C) +AT led to a promising EI of 6% and UTS of 690 MPa at 650 °C. While the main acicular O and discontinuous GB O+α_2 in the sample after SHT (1000 °C) +AT led to a promising UTS of 820 MPa and EI of 3% at 650 °C.
4. This paper mainly focuses on the effects of SHT temperature on the microstructure and mechanical properties of the SLMed Ti_2AlNb samples. Future research will be conducted on the effect of aging temperature for the SLMed Ti_2AlNb intermetallic.

CRediT authorship contribution statement

Xiuxuan Yang: Conceptualization, Methodology, Data curation, Writing – original draft. **Bi Zhang:** Supervision, Writing – review & editing, Funding acquisition. **Qian Bai:** Conceptualization, Writing – review & editing, Funding acquisition, Investigation. **Guoyin Xie:** Resources, Validation.

Declaration of competing interest

The authors declare that they have no known competing financial interests or personal relationships that could have appeared to influence the work reported in this paper.

Acknowledgements

The financial supports from the National Natural Science Foundation of China, China (52175381, 51605077) and the Peacock Program of Shenzhen, China (KQJSCX20180322152221965) are gratefully acknowledged.

References

[1] H. Zhao, B. Lu, M. Tong, R. Yang, Tensile behavior of Ti-22Al-24Nb-0.5Mo in the range 25–650°C [J], Mater. Sci. Eng., A 679 (2017) 455–464.
[2] J. Wu, R. Guo, L. Xu, Z. Lu, Y. Cui, R. Yang, Effect of hot isostatic pressing loading route on microstructure and mechanical properties of powder metallurgy Ti2AlNb alloys [J], J. Mater. Sci. Technol. 33 (2) (2017) 172–178.
[3] G. Wang, J. Yang, X. Jiao, Microstructure and mechanical properties of Ti–22Al–25Nb intermetallic fabricated by elemental powder metallurgy [J], Mater. Sci. Eng., A 654 (2016) 69–76.
[4] K. Muraleedharan, T.K. Nandy, D. Banerjee, S. Lele, Phase stability and ordering behaviour of the O phase in TiAlNb alloys [J], Intermetallics 3 (3) (1995) 187–199.
[5] L. Germann, D. Banerjee, J.Y. Guédou, J.L. Strudel, Effect of composition on the mechanical properties of newly developed Ti2AlNb-based titanium aluminide [J], Intermetallics 13 (9) (2005) 920–924.
[6] P. Lin, Z. He, S. Yuan, J. Shen, Y. Huang, X. Liang, Instability of the O-phase in Ti–22Al–25Nb alloy during elevated-temperature deformation [J], J. Alloys Compd. 578 (2013) 96–102.
[7] C. Xue, W. Zeng, B. Xu, X. Liang, J. Zhang, S. Li, B2 grain growth and particle pinning effect of Ti-22Al-25Nb orthorhombic intermetallic alloy during heating process [J], Intermetallics 29 (2012) 41–47.
[8] T. DebRoy, H.L. Wei, J.S. Zuback, et al., Additive manufacturing of metallic components–process, structure and properties[J], Prog. Mater. Sci. 92 (2018) 112–224.
[9] Y.P. Dong, Y.L. Li, S.Y. Zhou, et al., Cost-affordable Ti-6Al-4V for additive manufacturing: powder modification, compositional modulation and laser in-situ alloying[J], Additive Manufacturing 37 (2021) 101699.
[10] Y. Hou, B. Liu, Y. Liu, et al., Ultra-low cost Ti powder for selective laser melting additive manufacturing and superior mechanical properties associated[J], Opto-Electronic Advances 2 (5) (2019), 180028-1-180028-8.
[11] A. Grigoriev, I. Polozov, V. Sufiiarov, A. Popovich, In-situ synthesis of Ti2AlNb-based intermetallic alloy by selective laser melting [J], J. Alloys Compd. 704 (2017) 434–442.
[12] Y.H. Zhou, W.P. Li, D.W. Wang, L. Zhang, K. Ohara, J. Shen, T. Ebel, M. Yan, Selective laser melting enabled additive manufacturing of Ti–22Al–25Nb intermetallic: excellent combination of strength and ductility, and unique microstructural features associated [J], Acta Mater. 173 (2019) 117–129.
[13] C. Xue, W. Zeng, W. Wang, X. Liang, J. Zhang, Quantitative analysis on microstructure evolution and tensile property for the isothermally forged Ti2AlNb based intermetallic during heat treatment [J], Mater. Sci. Eng., A 573 (2013) 183–189.
[14] Z. Huang, P. Lin, J. Shen, Origin of the O phase and its effect on the mechanical properties of rolled Ti-22Al-25Nb alloy sheets [J], Mater. A. T. High. Temp. 38 (2) (2021) 103–113.
[15] Y. Zhang, Y. Liu, L. Yu, H. Liang, Y. Huang, Z. Ma, Microstructures and tensile properties of Ti2AlNb and Mo-modified Ti2AlNb alloys fabricated by hot isostatic pressing [J], Mater. Sci. Eng., A 776 (2020) 139043.
[16] X. Jiao, B. Kong, W. Tao, G. Liu, H. Ning, Effects of annealing on microstructure and deformation uniformity of Ti-22Al-24Nb-0.5Mo laser-welded joints [J], Mater. Des. 130 (2017) 166–174.
[17] W. Chen, Z.Y. Chen, C.C. Wu, J.W. Li, Z.Y. Tang, Q.J. Wang, The effect of annealing on microstructure and tensile properties of Ti–22Al–25Nb electron beam weld joint [J], Intermetallics 75 (2016) 8–14.
[18] W. Wang, W. Zeng, C. Xue, X. Liang, J. Zhang, Microstructure control and mechanical properties from isothermal forging and heat treatment of Ti–22Al–25Nb (at.%) orthorhombic alloy [J], Intermetallics 56 (2015) 79–86.
[19] C. Kenel, K. Dawson, J. Barras, C. Hauser, G. Dasargyri, T. Bauer, A. Colella, A. B. Spierings, G.J. Tatlock, C. Leinenbach, K. Wegener, Microstructure and oxide particle stability in a novel ODS γ-TiAl alloy processed by spark plasma sintering and laser additive manufacturing [J], Intermetallics 90 (2017) 63–73.
[20] Y.H. Zhou, D.W. Wang, L.J. Song, A. Mukhtar, D.N. Huang, C. Yang, M. Yan, Effect of heat treatments on the microstructure and mechanical properties of Ti2AlNb intermetallic fabricated by selective laser melting [J], Mater. Sci. Eng., A 817 (2021) 141352.
[21] S.L. Sing, S. Huang, G.D. Goh, et al., Emerging metallic systems for additive manufacturing: in-situ alloying and multi-metal processing in laser powder bed fusion[J], Prog. Mater. Sci. (2021) 100795.
[22] X. Nie, Z. Chen, Y. Qi, et al., Effect of defocusing distance on laser powder bed fusion of high strength Al–Cu–Mg–Mn alloy[J], Virtual Phys. Prototyp. 15 (3) (2020) 325–339.
[23] X.D. Nong, X.L. Zhou, Effect of scanning strategy on the microstructure, texture, and mechanical properties of 15-5PH stainless steel processed by selective laser melting[J], Mater. Char. 174 (2021) 111012.
[24] S.L. Sing, W.Y. Yeong, Laser powder bed fusion for metal additive manufacturing: perspectives on recent developments[J], Virtual Phys. Prototyp. 15 (3) (2020) 359–370.
[25] I. Polozov, V. Sufiiarov, A. Kantyukov, A. Popovich, Selective Laser Melting of Ti2AlNb-based intermetallic alloy using elemental powders: effect of process parameters and post-treatment on microstructure, composition, and properties [J], Intermetallics 112 (2019) 106554.
[26] J. Wu, L. Xu, Z. Lu, B. Lu, Y. Cui, R. Yang, Microstructure design and heat response of powder metallurgy Ti2AlNb intermetallics [J], J. Mater. Sci. Technol. 31 (12) (2015) 1251–1257.
[27] S. Huang, R.L. Narayan, J.H.K. Tan, et al., Resolving the porosity-unmelted inclusion dilemma during in-situ alloying of Ti34Nb via laser powder bed fusion [J], Acta Mater. 204 (2021) 116522.
[28] Q. Bai, B. Wu, X. Qiu, Bi Zhang, Experimental study on additive/subtractive hybrid manufacturing of 6511 steel: process optimization and machining characteristics [J], Int. J. Adv. Manuf. Technol. 108 (2020) 1389–1398.

[29] H. Wu, Y. Ren, J. Ren, et al., Effect of melting modes on microstructure and tribological properties of selective laser melted AlSi10Mg alloy[J], Virtual Phys. Prototyp. 15 (sup1) (2020) 570–582.
[30] Y. Wang, J. Shi, Y. Liu, Competitive grain growth and dendrite morphology evolution in selective laser melting of Inconel 718 superalloy [J], J. Cryst. Growth 521 (2019) 15–29.
[31] C.J. Boehlert, B.S. Majumdar, V. Seetharaman, D.B. Miracle, Part I. The microstructural evolution in Ti-Al-Nb O+Bcc orthorhombic alloys [J], Metall. Mater. Trans. 30 (9) (1999) 2305–2323.
[32] R.V. Chepulskii, S. Curtarolo, Calculation of solubility in titanium alloys from first principles [J], Acta Mater. 57 (18) (2009) 5314–5323.
[33] C. Xue, W. Zeng, W. Wang, X. Liang, J. Zhang, Quantitative analysis on microstructure evolution and tensile property for the isothermally forged Ti2AlNb based alloy during heat treatment [J], Mater. Sci. Eng., A 573 (2013) 183–189.
[34] K. Muraleedharan, A.K. Gogia, T.K. Nandy, et al., Transformations in a Ti-24AI-15Nb alloy: Part I. Phase equilibria and microstructure[J], Metallurgical Transactions A 23 (2) (1992) 401–415.
[35] W. Wang, W. Zeng, C. Xue, X. Liang, J. Zhang, Quantitative analysis of the effect of heat treatment on microstructural evolution and microhardness of an isothermally forged Ti–22Al–25Nb (at.%) orthorhombic alloy [J], Intermetallics 45 (2014) 29–37.
[36] K. Suardi, E. Hamzah, A. Ourdjini, V.C. Venkatesh, Effect of heat treatment on the diffusion coefficient of hydrogen absorption in gamma-titanium aluminide [J], J. Mater. Process. Technol. 185 (1) (2007) 106–112.
[37] M. Yetna N'Jock, D. Chicot, X. Decoopman, J. Lesage, J.M. Ndjaka, A. Pertuz, Mechanical tensile properties by spherical macroindentation using an indentation strain-hardening exponent [J], Int. J. Mech. Sci. 75 (2013) 257–264.
[38] C.H. Ward, Microstructure evolution and its effect on tensile and fracture behaviour of Ti-AI-Nb α2 intermetallics [J], Int. Mater. Rev. 38 (2) (1993) 79–101.
[39] H. Zhu, D.Y. Seo, K. Maruyama, P. Au, Effect of lamellar spacing on microstructural instability and creep behavior of a lamellar TiAl alloy [J], Scripta Mater. 54 (12) (2006) 1979–1984.